NANO LETTERS

pubs.acs.org/NanoLett Letter

Spatially Resolved Anion Diffusion and Tunable Waveguides in Bismuth Halide Perovskites

Yifeng Liu,[‖] Jingang Li,[*,‖] Yifan Zhu,[*,‖] Qing Ai, Rui Xu, Rundi Yang, Boyu Zhang, Qiyi Fang, Tianshu Zhai, Clyde Xu, Tanguy Terlier, Hanyu Zhu, Costas P. Grigoropoulos, and Jun Lou[*]

Cite This: *Nano Lett.* 2024, 24, 5182−5188 Read Online

ACCESS | Metrics & More | Article Recommendations | Supporting Information

ABSTRACT: Bismuth halide perovskites are widely regarded as nontoxic alternatives to lead halide perovskites for optoelectronics and solar energy harvesting applications. With a tailorable composition and intriguing optical properties, bismuth halide perovskites are also promising candidates for tunable photonic devices. However, robust control of the anion composition in bismuth halide perovskites remains elusive. Here, we established chemical vapor deposition and anion exchange protocols to synthesize bismuth halide perovskite nanoflakes with controlled dimensions and variable compositions. In particular, we demonstrated the gradient bromide distribution by controlling the anion exchange and diffusion processes, which is spatially resolved by time-of-flight secondary ion mass spectrometry. Moreover, the optical waveguiding properties of bismuth halide perovskites can be modulated by flake thicknesses and anion compositions. With a unique gradient anion distribution and controllable optical properties, bismuth halide perovskites provide new possibilities for applications in optoelectronic devices and integrated photonics.

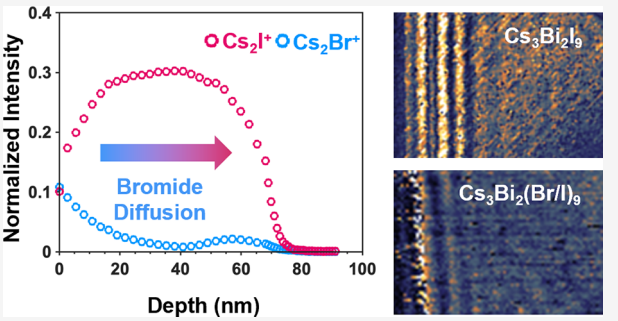

KEYWORDS: *Lead-free metal halide perovskites, anion exchange, anion diffusivity, waveguide, tunable optics, ultrathin crystals*

Metal halide perovskites (MHPs) have attracted intense attention due to their versatile applications in photovoltaics,[1,2] light-emitting diodes,[3,4] X-ray detectors,[5,6] lasers,[7,8] and photocatalysts.[9,10] Recently, lead-free MHPs have drawn considerable interest due to their nontoxicity and eco-friendliness.[11−13] Bismuth halide perovskites, a representative class of lead-free MHPs, have demonstrated great versatility in optoelectronic applications.[13−15] The intriguing valleytronics, electron−phonon couplings, and self-trapping states in bismuth halide perovskites further bring additional flexibilities in controlling the light−matter interactions with enhanced functionalities.[16−18]

Compositional engineering has been proven to be a promising method to control electronic band structures of MHPs, modify consequent optical properties, and further enhance the performance of MHP-based functional devices.[19−21] The composition at the halide sites in MHPs can be modulated by the stoichiometric control of halide precursors.[10,22] Alternatively, the high halide mobility in MHPs enables the postsynthetic anion exchange of parent perovskites with preserved crystal morphology.[20,23−26] Anion exchange with controllable diffusion processes also yields the gradient halide distribution in MHPs, which forms the energy funnel to facilitate charge carrier transport.[27−29]

In addition, anion exchange reactions provide an ideal platform to analyze the diffusion process in MHPs,[23,30,31] which is critical in stabilizing MHP heterostructures and devices with different compositions.[32−34] In lead halide perovskites, photoemission energies show a monotonic correlation with the anion ratio, which permits determination of the anion concentration from peak positions and intensities in photoluminescence (PL) spectra. One can further use this method to analyze the anion diffusion process and derive the diffusion coefficient.[26,34,35] However, unlike lead halide perovskites, bismuth halide perovskites with mixed anions (i.e., $Cs_3Bi_2(Br/Cl)_xI_{9-x}$) exhibit a phase transition from a dimer structure to a layered structure when $x > 3$.[15,18] Therefore, the band energy level and PL emission are synergistically determined by both the lattice structure and the anion composition.[15] In addition, indirect band gap, self-trapping emission, and electron−phonon coupling in bismuth halide perovskites lead to broad and overlapping PL emission bands.[16,18,36] These features require new approaches, instead of PL measurements, for reliable diffusion analysis in bismuth halide perovskites.

Received: January 23, 2024
Revised: April 10, 2024
Accepted: April 11, 2024
Published: April 17, 2024

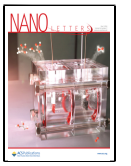

https://doi.org/10.1021/acs.nanolett.4c00327
Nano Lett. 2024, 24, 5182−5188

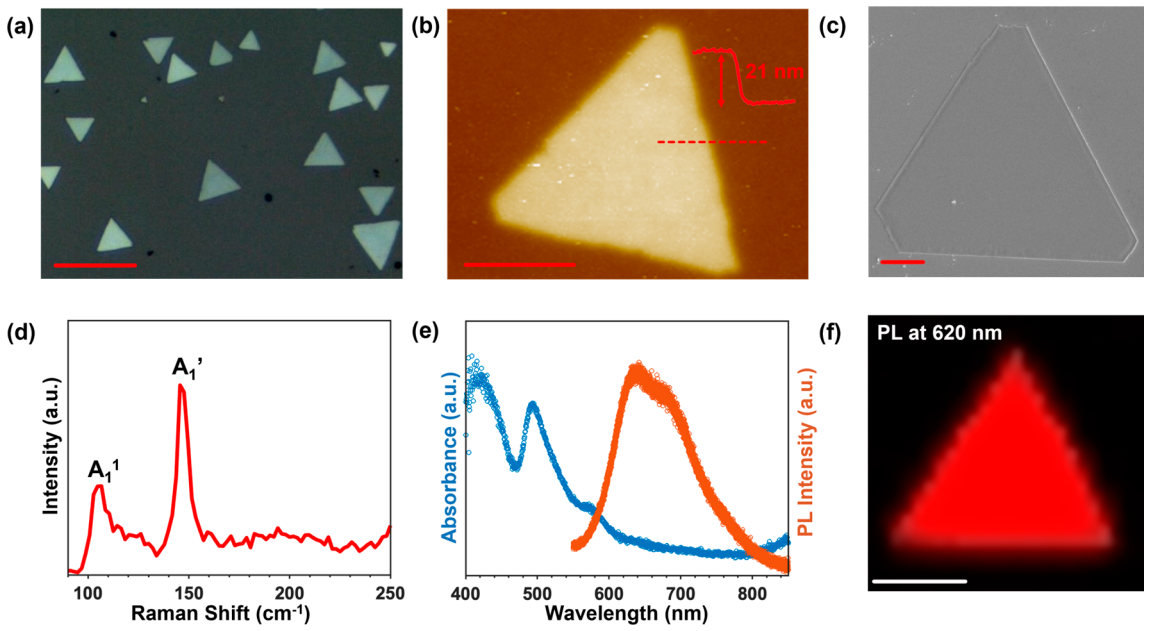

Figure 1. Characterizations of CVD-grown $Cs_3Bi_2I_9$. (a) Representative optical image of the $Cs_3Bi_2I_9$ flakes on the Mica substrates. Scale bar: 50 μm. (b) Representative AFM image of a $Cs_3Bi_2I_9$ flake. The inset height profile shows a thickness of ~21 nm. Scale bar: 10 μm. (c) SEM image of a $Cs_3Bi_2I_9$ flake. Scale bar: 2 μm. (d) Raman spectrum of the $Cs_3Bi_2I_9$ perovskites. (e) Absorption and PL (excitation: 532 nm) spectra of the $Cs_3Bi_2I_9$ perovskites. (f) PL mapping at 620 nm of a $Cs_3Bi_2I_9$ perovskite flake. Scale bar: 20 μm.

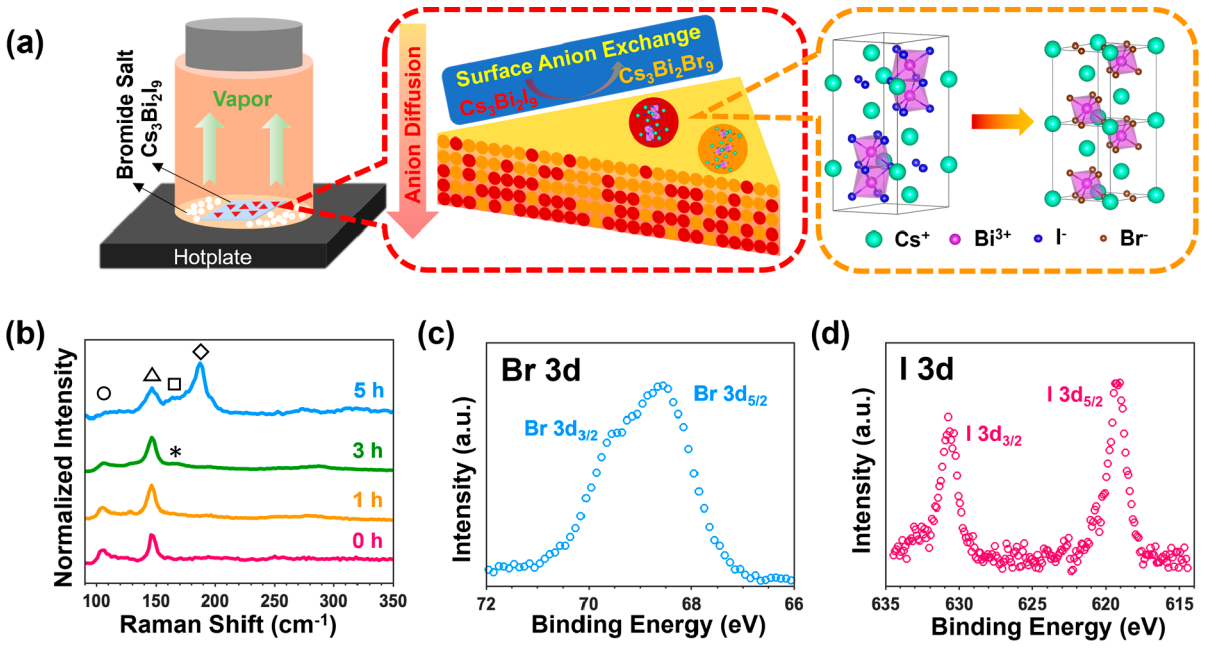

Figure 2. Anion exchange in bismuth halide perovskites. (a) Left: schematic illustration of the postsynthesis vapor phase anion exchange setup. Middle: schematic illustration of the anion exchange mechanism involving the surface anion exchange reaction and vertical anion diffusion processes. Right: lattice structures of $Cs_3Bi_2I_9$ (dimer, $P6_3/mmc$) and $Cs_3Bi_2Br_9$ (layer, $P\bar{3}m1$). (b) Raman spectra of the bromide exchanged $Cs_3Bi_2I_9$ perovskites with different reaction times. The thickness of the tested perovskite flakes is controlled to be around 30 nm. Circle: Bi−I $A_1{}^1$ mode. Triangle: Bi−I $A_1{}'$ mode. Square: Bi−Br E_g mode. Diamond: Bi−Br A_{1g} mode. Asterisk: combination of Bi−Br E_g and A_{1g} modes. XPS spectra of (c) Br 3d and (d) I 3d scans of $Cs_3Bi_2(Br/I)_9$ (3 h) perovskites.

Here, we prepare bismuth halide perovskites with tunable optical properties and analyze the anion diffusivity. In our previous work, we reported the growth of ultrathin and high-quality cesium bismuth iodide ($Cs_3Bi_2I_9$) perovskite nanoflakes by a chemical vapor deposition (CVD) method.[17] Through a postsynthetic anion exchange process, we synthesize $Cs_3Bi_2(Br/I)_9$ perovskites with gradient bromide distributions. We measure the bromide distribution by time-of-flight secondary ion mass spectrometry (ToF-SIMS) and determine the anion diffusivity to be $(1.56 \pm 0.17) \times 10^{-19}$ m^2/s at 100 °C. Additionally, we employ a scattering-type scanning near-field optical microscope (s-SNOM) to investigate optical waveguiding properties in bismuth halide perovskites. The waveguiding characteristics can be effectively modulated by

https://doi.org/10.1021/acs.nanolett.4c00327
Nano Lett. 2024, 24, 5182−5188

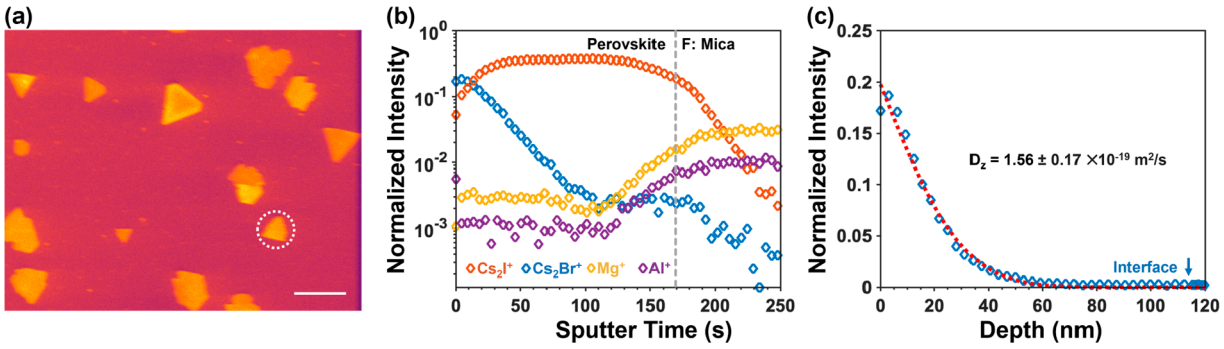

Figure 3. Anion diffusion in bismuth halide perovskites. (a) Total secondary ion image of the $Cs_3Bi_2(Br/I)_9$ perovskite flakes. The selected flake for anion diffusion analysis is marked by a dotted white circle. (b) ToF-SIMS depth profile of the selected flake. Cs_2Br^+ (blue) and Cs_2I^+ (orange) signals are from the perovskite flake. Mg^+ (yellow) and Al^+ (purple) signals are from the F: Mica substrate. The dashed gray line indicates the perovskite−substrate interface, which is determined at the half-maximum intensity of the Cs_2I^+. (c) Vertical bromide distribution in the selected flakes extracted from (b). The perovskite−substrate interface is labeled by the blue arrow.

controlling the crystal thickness or anion composition, highlighting their potential applications as photonic components. Along with the synthesis of $Cs_3Bi_2(Br/I)_9$ nanoflakes, the anion exchange protocol and diffusivity analysis reported in this work will provide important insights into the design and synthesis of other MHP materials.

Two-dimensional (2D) $Cs_3Bi_2I_9$ perovskites are prepared via a CVD growth method (Figure S1).[17] Briefly, CsI and BiI_3 powders are loaded on the upstream side of the quartz boat in front of the mica substrates. Mixed nitrogen/hydrogen gas is purged as the carrier gas and protected the system from the ambient atmosphere. The CVD furnace is heated to 620 °C for 1 h to yield $Cs_3Bi_2I_9$ perovskites. The as-synthesized $Cs_3Bi_2I_9$ perovskite flakes show triangular, truncated triangular, or hexagonal morphology with a lateral size of tens of micrometers (Figure 1a). The atomic force microscopy (AFM) measurement reveals the smooth surface of perovskite flakes (Figure 1b), and the thicknesses can vary from less than 10 nm to over 100 nm. The high quality of the $Cs_3Bi_2I_9$ perovskite crystals is further confirmed by the scanning electron microscope (SEM) image (Figure 1c).

The phase of $Cs_3Bi_2I_9$ crystals is characterized by Raman spectroscopy (Figure 1d), where the peaks at 106 and 147 cm^{-1} can be assigned to the Bi−I bridging (A_1^1 mode) and terminal (A_1' mode) stretching of the dimer phase ($P6_3/mmc$) $Cs_3Bi_2I_9$ perovskites. The excitonic characteristics and optical properties of the $Cs_3Bi_2I_9$ perovskite flakes have been studied by absorption and PL spectra. The absorption spectrum presents a dominant first excitonic peak at around 490 nm (Figure 1e) and another weak peak at around 570 nm, which may originate from the second excitation with higher binding energy.[37] The exciton corresponding to the peak at 570 nm can also originate from the degenerate conduction bands, considering the spin−orbit couplings.[37] The two excitonic peaks with ∼0.36 eV separation match the previous experimental results and DFT calculations.[37−39] A broad PL emission peak ranging from 570 to 770 nm can be observed (Figure 1e), suggesting the existence of multiple luminescence peaks. The broadened and multiple photoemissions can be ascribed to self-trapping states, direct and indirect band gaps, and electron−phonon couplings in the $Cs_3Bi_2I_9$ perovskites.[18,36,37] PL mapping of the signature photoemission peak of $Cs_3Bi_2I_9$ perovskites centered at 620 nm (Figure 1f) shows uniform light emission from the entire flake, indicating high crystallinity and fewer defects in the synthesized $Cs_3Bi_2I_9$ perovskites.

$Cs_3Bi_2(Br/I)_9$ perovskite flakes are prepared from $Cs_3Bi_2I_9$ flakes through a postsynthesis anion exchange process in the vapor phase. As illustrated in Figure 2a, the substrates with presynthesized $Cs_3Bi_2I_9$ are placed into vials loaded with bromide precursors (methylammonium bromide (MABr), butylammonium bromide (BABr), or bismuth(III) bromide ($BiBr_3$)). The capped vials are heated to 150 °C with different reaction time periods to yield bromide-exchanged $Cs_3Bi_2(Br/I)_9$ perovskite crystals. The evolution of the bromide formation through the anion exchange process with MABr treatment is monitored by Raman spectra (Figure 2b and Figure S2). The Raman spectrum of $Cs_3Bi_2(Br/I)_9$ (1 h) does not show significant differences from that of the pristine $Cs_3Bi_2I_9$ (0 h). After a 3 h reaction, an emerging Raman peak at around 165 cm^{-1} appears (green curve), which is considered as the signature of the combined Bi−Br E_g and A_{1g} stretching in $Cs_3Bi_2(Br/I)_9$.[40,41] After 5 h, the Raman spectrum of $Cs_3Bi_2(Br/I)_9$ (5 h) perovskite (blue curve) presents peaks at both 165 cm^{-1} (Bi−Br E_g) and 191 cm^{-1} (Bi−Br A_{1g} mode), as well as the vanishing of the Bi−I A_1^1 mode at 106 cm^{-1}, indicating the formation of $Cs_3Bi_2Br_9$ perovskite components. Meanwhile, the remaining Bi−I A_1' mode at 147 cm^{-1} indicates that the anion exchange is still incomplete. Anion exchange processes with different precursors are also monitored under controlled temperature, reaction time, and sample thickness conditions (Figure S3). Compared to organic bromide precursors, $Cs_3Bi_2I_9$ perovskites treated with the $BiBr_3$ precursor show more efficient bromide exchange with clearer characteristic Raman peaks from $Cs_3Bi_2Br_9$. We attribute this result to the relatively low melting point of $BiBr_3$, which will be vaporized faster to reach concentration equilibrium in the closed vials and accelerate the surface anion exchange reaction.

In addition to the surface reaction (from $Cs_3Bi_2I_9$ to $Cs_3Bi_2Br_9$), the anion exchange also involves vertical anion diffusion (bromide diffuses from concentrated surface to the diluted bulk side, Figure 2a). Such gradient bromide distribution provides an ideal platform for us to study the anion diffusion in bismuth halide perovskites. We first characterize the surface chemical composition of the $Cs_3Bi_2(Br/I)_9$ (3 h) and pristine $Cs_3Bi_2I_9$ perovskites by X-ray photoemission spectroscopy (XPS) (Figure S5). The existence of both bromide and iodide in the $Cs_3Bi_2(Br/I)_9$ (3 h) perovskite is confirmed from the XPS Br 3d (Figure 2c) and

https://doi.org/10.1021/acs.nanolett.4c00327
Nano Lett. 2024, 24, 5182−5188

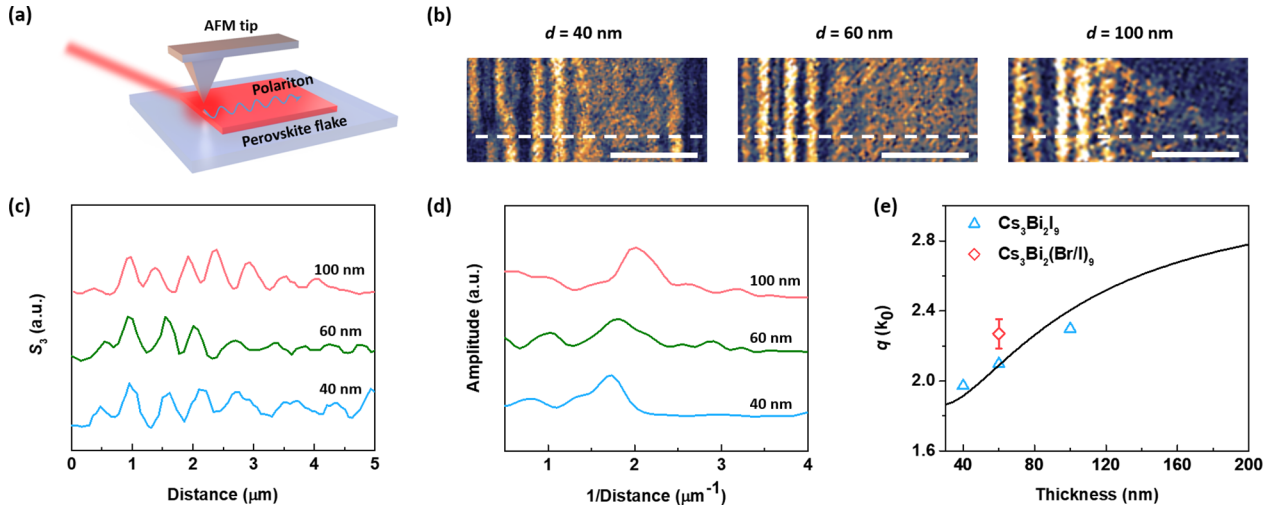

Figure 4. Near-field nanoimaging of waveguiding modes in bismuth halide perovskites. (a) Schematic showing the near-field imaging of perovskite waveguides. (b) Near-field images of $Cs_3Bi_2I_9$ flakes with thicknesses d of 40, 60, and 100 nm. Scale bars: 2 μm. (c) Real-space fringe profiles and (d) corresponding FT profiles extracted from (b). (e) Experimental (dots) and theoretical (line) thickness dispersions of the TE_0 waveguide mode. The red dot shows the experimental results of $Cs_3Bi_2(Br/I)_9$ perovskite flakes.

I 3d (Figure 2d) scans. The average bromide-to-iodide ratio is estimated to be 5.9 (85.49% of Br to 14.51% of I), indicating a bromide-rich surface after the surface anion exchange process. Subsequently, we apply the ToF-SIMS technique to measure the distribution of bromide and iodide in the $Cs_3Bi_2(Br/I)_9$ (3 h) perovskites (Figure S8). The bromide species (Cs_2Br^+, Figure S8a) are concentrated on the surface while more iodide species (Cs_2I^+, Figure S8b) exist in the bulk crystals (Figure S8d). The gradient distribution of Cs_2Br^+ along the out-of-plane direction can be clearly visualized from the depth profile (Figure S9). The intensity of Cs_2Br^+ declines from the crystal surface to the bulk region due to anion diffusion. Interestingly, we also observe a small peak of the Cs_2Br^+ intensity at the perovskite−substrate interface. One possible reason is the intercalation of the bromide precursor into the gap between the perovskite and substrate to trigger anion exchange on the bottom side.

The ToF-SIMS depth profile of normalized intensity from different ionic fragments enables a quantitative analysis of the anion diffusivity in the thickness direction in bismuth halide perovskites with nanoscale spatial resolution. We consider the anion exchange in this study as one-dimensional (1D) semi-infinite diffusion from the crystal surface to the substrate, which can be quantified using Fick's second law (see Supplementary Note). To avoid the complicated condition where diffusion reaches the sample−substrate interface, we study a thick crystal (>100 nm thickness) and mild reaction conditions ($BiBr_3$ as bromide precursor, reaction temperature of 100 °C, reaction time of 30 min). Figure 3a shows the ToF-SIMS image of the $Cs_3Bi_2(Br/I)_9$ perovskite crystals, and the corresponding depth profile of a selected perovskite crystal is plotted in Figure 3b. The vertical distribution of bromide is extracted and fitted with Fick's second law (Figure 3c)

$$I = k \times \left(1 - \mathrm{erf}\left(\frac{l}{2\sqrt{Dt}}\right)\right) \quad (1)$$

where I is the normalized ToF-SIMS intensity, l is the diffusion length, D is the diffusion coefficient, t is the reaction time, and k is a fitting parameter. We determine the vertical bromide diffusivity in bismuth halide perovskites to be (1.56 ± 0.17) × 10^{-19} m^2/s at 100 °C. The average diffusion coefficient of the total 9 selected flakes has been further determined to be 1.55 × 10^{-19} m^2/s (Figure S10 and Table S1), which is 1 order of magnitude slower than that in lead halide perovskites (~10^{-18} m^2/s).[25] We hypothesize that the isolated $[Bi_2I_9]^{3-}$ dimer structures in the perovskite lattices may hinder anion diffusion among those dimer clusters due to the lack of interconnecting bonds. Structure-dependent diffusion has also been observed in 2D organic−inorganic hybrid lead halide perovskites where the interlayer organic spacers can impede the anion diffusion and result in lower anion diffusivities compared to the quasi 2D and 3D counterparts.[34,42]

Next, we used the near-field nanoimaging technique, s-SNOM, to investigate the optical waveguiding properties of bismuth halide perovskites (Figure 4a). Compared with far-field methods, s-SNOM enables the direct visualization of real-space distribution and propagation of localized electromagnetic fields with a nanoscale resolution.[43−45] Here, a near-infrared laser beam with a wavelength of 800 nm is used to excite the waveguide modes. Figure 4b shows the near-field images of $Cs_3Bi_2I_9$ perovskite flakes with different thicknesses of approximately 40, 60, and 100 nm (measured by AFM). Fringe patterns parallel to the crystal edges can be observed due to the interference between the tip-scattered light and edge-scattered photons. The in-plane optical wavevector q of the perovskite waveguide can be calculated from the period of the fringes (ρ)[46,47]

$$q = \frac{\lambda_0}{\rho} k_0 + k_0 \cos\alpha \cos\theta \quad (2)$$

where λ_0 and k_0 are the incident laser wavelength and wavevector, respectively, θ is the incident angle, and $k_0 \cos\alpha$ is in-plane component of the incident wavevector (Figure S13).

We then extract the real-space profiles of the fringe patterns from near-field images (Figure 4c) and apply Fourier transform (FT) to accurately determine the fringe periods (Figure 4d). The peaks in the FT profiles correspond to the wavevector of the transverse electric mode (TE_0), which shifts to higher frequencies with the increasing thickness (Figure 4e). We also calculate the theoretical wavevectors of TE modes using the

https://doi.org/10.1021/acs.nanolett.4c00327
Nano Lett. 2024, 24, 5182−5188

planar waveguide model,[48] which match well with the experimental thickness dispersion. The corresponding wavelengths (λ_p) of the waveguide modes are determined to be 405.8, 381.3, and 348.1 nm in $Cs_3Bi_2I_9$ perovskites with thicknesses of 40, 60, and 100 nm, respectively. λ_p is shorter than half of the incident wavelength in ultrathin $Cs_3Bi_2I_9$ perovskite flakes of less than 100 nm thickness, indicating efficient confinement of electromagnetic fields at the subwavelength scale. We further perform an inverse Fourier transform to the FT profile after filtering out the short (<1 μm^{-1}) and long (>3 μm^{-1}) spatial frequencies to determine the propagation length Lp of the waveguide mode. By fitting the new profile with an exponentially decaying envelope, we obtain Lp ≈ 2 μm (Figure S15), which is similar to those of 2D transition metal dichalcogenide waveguides.[47] The challenge of achieving longer propagation length in our perovskite waveguides may be ascribed to the losses from surface roughness and nonuniformity.

Finally, we demonstrate additional tunability of the waveguide properties by anion exchange. The mixed-anion $Cs_3Bi_2(Br/I)_9$ and pristine $Cs_3Bi_2I_9$ perovskite flakes with a similar thickness of 60 nm are selected. The absence of the Bi−Br stretching in the Raman spectrum indicates an overall low bromide concentration in $Cs_3Bi_2(Br/I)_9$ perovskites (Figure S14). With such mild compositional modification, we observe distinct waveguide performances compared with the pristine perovskite flakes. By analyzing the s-SNOM profiles of $Cs_3Bi_2(Br/I)_9$ and $Cs_3Bi_2I_9$ perovskites (Figure S16), we determine a larger wavevector in the 60 nm $Cs_3Bi_2(Br/I)_9$ flake and a more confined λ_p of 352.6 nm (Figure 4e). These results indicate the effectiveness of compositional engineering in the modulation of functionalities of bismuth halide perovskites. Our postsynthetic anion exchange provides a promising pathway for developing active and tunable photonic devices based on MHPs.

In summary, we investigate anion diffusion and tunable waveguide performances in bismuth halide perovskites. A postsynthetic anion exchange protocol is established to prepare mixed anion $Cs_3Bi_2(Br/I)_9$ perovskites from the pristine $Cs_3Bi_2I_9$ perovskites. The spatial-resolved gradient anion distribution is characterized by the ToF-SIMS technique to determine the vertical bromide diffusivity. We then apply the near-field nanoimaging technique to study the photonic waveguide performances, which can be controlled by the crystal thickness and anion composition. It is clearly shown that compositional modification by anion exchange presents an effective strategy to modulate the optical properties of bismuth halide perovskites. With added flexibility in optical properties by anion exchange, our work highlights the potential for various photonic applications and provides a general approach for the future innovation of MHP materials and devices.

■ ASSOCIATED CONTENT

Supporting Information

The Supporting Information is available free of charge at https://pubs.acs.org/doi/10.1021/acs.nanolett.4c00327.

Experimental methods, sample characterizations of the ultrathin bismuth halide perovskites, schematic of the CVD growth of $Cs_3Bi_2I_9$, schematic of the s-SNOM setup and waveguide performance of the mixed anion bismuth halide perovskites, and supplementary notes of the anion diffusivity analysis and optical characterizations (PDF)

■ AUTHOR INFORMATION

Corresponding Authors

Jingang Li − *Laser Thermal Laboratory, Department of Mechanical Engineering, University of California, Berkeley, California 94720, United States;* orcid.org/0000-0003-0827-9758; Email: jingang@berkeley.edu

Yifan Zhu − *Department of Materials Science and NanoEngineering, Rice University, Houston, Texas 77005, United States;* orcid.org/0000-0002-9816-5764; Email: yifan.zhu@rice.edu

Jun Lou − *Department of Materials Science and NanoEngineering, Rice University, Houston, Texas 77005, United States;* orcid.org/0000-0002-4351-9561; Email: jlou@rice.edu

Authors

Yifeng Liu − *Department of Materials Science and NanoEngineering, Rice University, Houston, Texas 77005, United States*

Qing Ai − *Department of Materials Science and NanoEngineering, Rice University, Houston, Texas 77005, United States;* orcid.org/0000-0002-6086-5431

Rui Xu − *Department of Materials Science and NanoEngineering, Rice University, Houston, Texas 77005, United States;* orcid.org/0000-0002-7072-1976

Rundi Yang − *Laser Thermal Laboratory, Department of Mechanical Engineering, University of California, Berkeley, California 94720, United States;* orcid.org/0000-0002-2877-939X

Boyu Zhang − *Department of Materials Science and NanoEngineering, Rice University, Houston, Texas 77005, United States*

Qiyi Fang − *Department of Materials Science and NanoEngineering, Rice University, Houston, Texas 77005, United States*

Tianshu Zhai − *Department of Materials Science and NanoEngineering, Rice University, Houston, Texas 77005, United States*

Clyde Xu − *Department of Materials Science and NanoEngineering, Rice University, Houston, Texas 77005, United States*

Tanguy Terlier − *SIMS Laboratory, Shared Equipment Authority, Rice University, Houston, Texas 77005, United States;* orcid.org/0000-0002-4092-0771

Hanyu Zhu − *Department of Materials Science and NanoEngineering, Rice University, Houston, Texas 77005, United States;* orcid.org/0000-0003-3376-5352

Costas P. Grigoropoulos − *Laser Thermal Laboratory, Department of Mechanical Engineering, University of California, Berkeley, California 94720, United States;* orcid.org/0000-0002-8505-4037

Complete contact information is available at: https://pubs.acs.org/10.1021/acs.nanolett.4c00327

Author Contributions

[‖]Y.L., J.Li., and Y.Z. contributed equally.

Notes

The authors declare no competing financial interest.

https://doi.org/10.1021/acs.nanolett.4c00327
Nano Lett. 2024, 24, 5182−5188

■ ACKNOWLEDGMENTS

The work was supported by the Welch Foundation (Grant C-1716) and the NSF I/UCRC Center for Atomically Thin Multifunctional Coatings (ATOMIC) under award # EEC-2113882. C.P.G. acknowledges financial support from the National Science Foundation (Grant No. CMMI-2024391) and U.S. Department of Energy through Laser Prismatics LLC (Grant No. SBIR/STTR DE-SC0018461). ToF-SIMS analysis was carried out with support provided by the National Science Foundation CBET-1626418. R.X. and H.Z. acknowledge the Welch Foundation (Grant No. C-2128). This work was conducted in part using resources of the Shared Equipment Authority at Rice University.

■ REFERENCES

(1) Kojima, A.; Teshima, K.; Shirai, Y.; Miyasaka, T. Organometal Halide Perovskites as Visible-Light Sensitizers for Photovoltaic Cells. *J. Am. Chem. Soc.* **2009**, *131*, 6050−6051.
(2) Lin, Y. H.; Sakai, N.; Da, P.; Wu, J.; Sansom, H. C.; Ramadan, A. J.; Mahesh, S.; Liu, J.; Oliver, R. D. J.; Lim, J.; Aspitarte, L.; Sharma, K.; Madhu, P. K.; Morales-Vilches, A. B.; Nayak, P. K.; Bai, S.; Gao, F.; Grovenor, C. R. M.; Johnston, M. B.; Labram, J. G.; Durrant, J. R.; Ball, J. M.; Wenger, B.; Stannowski, B.; Snaith, H. J. A Piperidinium Salt Stabilizes Efficient Metal-Halide Perovskite Solar Cells. *Science (80-.).* **2020**, *369*, 96−102.
(3) Lin, K.; Xing, J.; Quan, L. N.; de Arquer, F. P. G.; Gong, X.; Lu, J.; Xie, L.; Zhao, W.; Zhang, D.; Yan, C.; Li, W.; Liu, X.; Lu, Y.; Kirman, J.; Sargent, E. H.; Xiong, Q.; Wei, Z. Perovskite Light-Emitting Diodes with External Quantum Efficiency Exceeding 20 per Cent. *Nature* **2018**, *562*, 245−248.
(4) Xu, W.; Hu, Q.; Bai, S.; Bao, C.; Miao, Y.; Yuan, Z.; Borzda, T.; Barker, A. J.; Tyukalova, E.; Hu, Z.; Kawecki, M.; Wang, H.; Yan, Z.; Liu, X.; Shi, X.; Uvdal, K.; Fahlman, M.; Zhang, W.; Duchamp, M.; Liu, J. M.; Petrozza, A.; Wang, J.; Liu, L. M.; Huang, W.; Gao, F. Rational Molecular Passivation for High-Performance Perovskite Light-Emitting Diodes. *Nat. Photonics* **2019**, *13*, 418−424.
(5) Wei, H.; Fang, Y.; Mulligan, P.; Chuirazzi, W.; Fang, H. H.; Wang, C.; Ecker, B. R.; Gao, Y.; Loi, M. A.; Cao, L.; Huang, J. Sensitive X-Ray Detectors Made of Methylammonium Lead Tribromide Perovskite Single Crystals. *Nat. Photonics* **2016**, *10*, 333−339.
(6) Deumel, S.; van Breemen, A.; Gelinck, G.; Peeters, B.; Maas, J.; Verbeek, R.; Shanmugam, S.; Akkerman, H.; Meulenkamp, E.; Huerdler, J. E.; Acharya, M.; García-Batlle, M.; Almora, O.; Guerrero, A.; Garcia-Belmonte, G.; Heiss, W.; Schmidt, O.; Tedde, S. F. High-Sensitivity High-Resolution X-Ray Imaging with Soft-Sintered Metal Halide Perovskites. *Nat. Electron.* **2021**, *4*, 681−688.
(7) Zhu, H.; Fu, Y.; Meng, F.; Wu, X.; Gong, Z.; Ding, Q.; Gustafsson, M. V.; Trinh, M. T.; Jin, S.; Zhu, X. Y. Lead Halide Perovskite Nanowire Lasers with Low Lasing Thresholds and High Quality Factors. *Nat. Mater.* **2015**, *14*, 636−642.
(8) Jia, Y.; Kerner, R. A.; Grede, A. J.; Rand, B. P.; Giebink, N. C. Continuous-Wave Lasing in an Organic-Inorganic Lead Halide Perovskite Semiconductor. *Nat. Photonics* **2017**, *11*, 784−788.
(9) Park, S.; Chang, W. J.; Lee, C. W.; Park, S.; Ahn, H. Y.; Nam, K. T. Photocatalytic Hydrogen Generation from Hydriodic Acid Using Methylammonium Lead Iodide in Dynamic Equilibrium with Aqueous Solution. *Nat. Energy* **2017**, *2*, 1−8.
(10) Zhu, Y.; Liu, Y.; Miller, K. A.; Zhu, H.; Egap, E. Lead Halide Perovskite Nanocrystals as Photocatalysts for PET-RAFT Polymerization under Visible and Near-Infrared Irradiation. *ACS Macro Lett.* **2020**, *9*, 725−730.
(11) Han, X.; Liang, J.; Yang, J. H.; Soni, K.; Fang, Q.; Wang, W.; Zhang, J.; Jia, S.; Martí, A. A.; Zhao, Y.; Lou, J. Lead-Free Double Perovskite Cs2SnX6: Facile Solution Synthesis and Excellent Stability. *Small* **2019**, *15*, 1−7.
(12) Liang, J.; Soni, K.; Lou, J. Morphology Evolution of Ultra-Stable and Low-Cost All-Inorganic Lead-Free Perovskite Solar Cells. *Mater. Today Energy* **2023**, *32*, No. 101241.
(13) Yang, B.; Chen, J.; Hong, F.; Mao, X.; Zheng, K.; Yang, S.; Li, Y.; Pullerits, T.; Deng, W.; Han, K. Lead-Free, Air-Stable All-Inorganic Cesium Bismuth Halide Perovskite Nanocrystals. *Angew. Chemie - Int. Ed.* **2017**, *56*, 12471−12475.
(14) Zhang, Y.; Liu, Y.; Xu, Z.; Ye, H.; Yang, Z.; You, J.; Liu, M.; He, Y.; Kanatzidis, M. G.; Liu, S. (Frank). Nucleation-Controlled Growth of Superior Lead-Free Perovskite Cs3Bi2I9 Single-Crystals for High-Performance X-Ray Detection. *Nat. Commun.* **2020**, *11*, 1−11.
(15) Yu, B.-B.; Liao, M.; Yang, J.; Chen, W.; Zhu, Y.; Zhang, X.; Duan, T.; Yao, W.; Wei, S.-H.; He, Z. Alloy-Induced Phase Transition and Enhanced Photovoltaic Performance: The Case of Cs3Bi2I9-XBrx Perovskite Solar Cells. *J. Mater. Chem. A* **2019**, *7*, 8818−8825.
(16) Zhou, L.; Liao, J.-F.; Qin, Y.; Wang, X.-D.; Wei, J.-H.; Li, M.; Kuang, D.-B.; He, R. Activation of Self-Trapped Emission in Stable Bismuth-Halide Perovskite by Suppressing Strong Exciton−Phonon Coupling. *Adv. Funct. Mater.* **2021**, *31*, No. 2102654.
(17) Liang, J.; Fang, Q.; Wang, H.; Xu, R.; Jia, S.; Guan, Y.; Ai, Q.; Gao, G.; Guo, H.; Shen, K.; Wen, X.; Terlier, T.; Wiederrecht, G. P.; Qian, X.; Zhu, H.; Lou, J. Perovskite-Derivative Valleytronics. *Adv. Mater.* **2020**, *32*, 1−7.
(18) McCall, K. M.; Stoumpos, C. C.; Kontsevoi, O. Y.; Alexander, G. C. B.; Wessels, B. W.; Kanatzidis, M. G. From 0D Cs 3 Bi 2 I 9 to 2D Cs 3 Bi 2 I 6 Cl 3 : Dimensional Expansion Induces a Direct Band Gap but Enhances Electron-Phonon Coupling. *Chem. Mater.* **2019**, *31*, 2644−2650.
(19) Lu, C. H.; Biesold-Mcgee, G. V.; Liu, Y.; Kang, Z.; Lin, Z. Doping and Ion Substitution in Colloidal Metal Halide Perovskite Nanocrystals. *Chem. Soc. Rev.* **2020**, *49*, 4953−5007.
(20) Shamsi, J.; Urban, A. S.; Imran, M.; De Trizio, L.; Manna, L. Metal Halide Perovskite Nanocrystals: Synthesis, Post-Synthesis Modifications, and Their Optical Properties. *Chem. Rev.* **2019**, *119*, 3296−3348.
(21) Ravi, V. K.; Markad, G. B.; Nag, A. Band Edge Energies and Excitonic Transition Probabilities of Colloidal CsPbX3 (X = Cl, Br, I) Perovskite Nanocrystals. *ACS Energy Lett.* **2016**, *1*, 665−671.
(22) Son, D. Y.; Kim, S. G.; Seo, J. Y.; Lee, S. H.; Shin, H.; Lee, D.; Park, N. G. Universal Approach toward Hysteresis-Free Perovskite Solar Cell via Defect Engineering. *J. Am. Chem. Soc.* **2018**, *140*, 1358−1364.
(23) Dou, L.; Lai, M.; Kley, C. S.; Yang, Y.; Bischak, C. G.; Zhang, D.; Eaton, S. W.; Ginsberg, N. S.; Yang, P. Spatially Resolved Multicolor CsPbX3 Nanowire Heterojunctions via Anion Exchange. *Proc. Natl. Acad. Sci. U. S. A.* **2017**, *114*, 7216−7221.
(24) Nedelcu, G.; Protesescu, L.; Yakunin, S.; Bodnarchuk, M. I.; Grotevent, M. J.; Kovalenko, M. V. Fast Anion-Exchange in Highly Luminescent Nanocrystals of Cesium Lead Halide Perovskites (CsPbX3, X = Cl, Br, I). *Nano Lett.* **2015**, *15*, 5635−5640.
(25) Elmelund, T.; Scheidt, R. A.; Seger, B.; Kamat, P. V. Bidirectional Halide Ion Exchange in Paired Lead Halide Perovskite Films with Thermal Activation. *ACS Energy Lett.* **2019**, *4*, 1961−1969.
(26) Zhang, Y.; Lu, D.; Gao, M.; Lai, M.; Lin, J.; Lei, T.; Lin, Z.; Quan, L. N.; Yang, P. Quantitative Imaging of Anion Exchange Kinetics in Halide Perovskites. *Proc. Natl. Acad. Sci. U. S. A.* **2019**, *116*, 12648−12653.
(27) Tang, Y.; Mak, C. H.; Wang, C.; Fu, Y.; Li, F. F.; Jia, G.; Hsieh, C. W.; Shen, H. H.; Colmenares, J. C.; Song, H.; Yuan, M.; Chen, Y.; Hsu, H. Y. Bandgap Funneling in Bismuth-Based Hybrid Perovskite Photocatalyst with Efficient Visible-Light-Driven Hydrogen Evolution. *Small Methods* **2022**, *6*, 1−9.
(28) Tian, W.; Leng, J.; Zhao, C.; Jin, S. Long-Distance Charge Carrier Funneling in Perovskite Nanowires Enabled by Built-in Halide Gradient. *J. Am. Chem. Soc.* **2017**, *139*, 579−582.
(29) Li, J.; Xu, J.; Bao, Y.; Li, J.; Wang, H.; He, C.; An, M.; Tang, H.; Sun, Z.; Fang, Y.; Liang, S.; Yang, Y. Anion-Exchange Driven Phase Transition in CsPbI3 Nanowires for Fabricating Epitaxial Perovskite Heterojunctions. *Adv. Mater.* **2022**, *34*, 1−9.

https://doi.org/10.1021/acs.nanolett.4c00327
Nano Lett. 2024, 24, 5182−5188

(30) Lai, M.; Obliger, A.; Lu, D.; Kley, C. S.; Bischak, C. G.; Kong, Q.; Lei, T.; Dou, L.; Ginsberg, N. S.; Limmer, D. T.; Yang, P. Intrinsic Anion Diffusivity in Lead Halide Perovskites Is Facilitated by a Soft Lattice. *Proc. Natl. Acad. Sci. U. S. A.* **2018**, *115*, 11929−11934.
(31) Roy, C. R.; Pan, D.; Wang, Y.; Hautzinger, M. P.; Zhao, Y.; Wright, J. C.; Zhu, Z.; Jin, S. Anion Exchange of Ruddlesden-Popper Lead Halide Perovskites Produces Stable Lateral Heterostructures. *J. Am. Chem. Soc.* **2021**, *143*, 5212−5221.
(32) Mao, W.; Hall, C. R.; Bernardi, S.; Cheng, Y. B.; Widmer-Cooper, A.; Smith, T. A.; Bach, U. Light-Induced Reversal of Ion Segregation in Mixed-Halide Perovskites. *Nat. Mater.* **2021**, *20*, 55−61.
(33) Kamat, P. V.; Kuno, M. Halide Ion Migration in Perovskite Nanocrystals and Nanostructures. *Acc. Chem. Res.* **2021**, *54*, 520−531.
(34) Akriti; Shi, E.; Shiring, S. B.; Yang, J.; Atencio-Martinez, C. L.; Yuan, B.; Hu, X.; Gao, Y.; Finkenauer, B. P.; Pistone, A. J.; Yu, Y.; Liao, P.; Savoie, B. M.; Dou, L. Layer-by-Layer Anionic Diffusion in Two-Dimensional Halide Perovskite Vertical Heterostructures. *Nat. Nanotechnol.* **2021**, *16*, 584−591.
(35) Pan, D.; Fu, Y.; Chen, J.; Czech, K. J.; Wright, J. C.; Jin, S. Visualization and Studies of Ion-Diffusion Kinetics in Cesium Lead Bromide Perovskite Nanowires. *Nano Lett.* **2018**, *18*, 1807−1813.
(36) Zhang, Y.; Yin, J.; Parida, M. R.; Ahmed, G. H.; Pan, J.; Bakr, O. M.; Brédas, J. L.; Mohammed, O. F. Direct-Indirect Nature of the Bandgap in Lead-Free Perovskite Nanocrystals. *J. Phys. Chem. Lett.* **2017**, *8*, 3173−3177.
(37) McCall, K. M.; Stoumpos, C. C.; Kostina, S. S.; Kanatzidis, M. G.; Wessels, B. W. Strong Electron-Phonon Coupling and Self-Trapped Excitons in the Defect Halide Perovskites A3M2I9 (A = Cs, Rb; M = Bi, Sb). *Chem. Mater.* **2017**, *29*, 4129−4145.
(38) Lehner, A. J.; Fabini, D. H.; Evans, H. A.; Hébert, C. A.; Smock, S. R.; Hu, J.; Wang, H.; Zwanziger, J. W.; Chabinyc, M. L.; Seshadri, R. Crystal and Electronic Structures of Complex Bismuth Iodides A3Bi2I9 (A = K, Rb, Cs) Related to Perovskite: Aiding the Rational Design of Photovoltaics. *Chem. Mater.* **2015**, *27*, 7137−7148.
(39) Pazoki, M.; Johansson, M. B.; Zhu, H.; Broqvist, P.; Edvinsson, T.; Boschloo, G.; Johansson, E. M. J. Bismuth Iodide Perovskite Materials for Solar Cell Applications: Electronic Structure, Optical Transitions, and Directional Charge Transport. *J. Phys. Chem. C* **2016**, *120*, 29039−29046.
(40) Ghosh, S.; Mukhopadhyay, S.; Paul, S.; Pradhan, B.; De, S. K. Control Synthesis and Alloying of Ambient Stable Pb-Free Cs3Bi2Br9(1- x)I9 x($0 \leq x \leq 1$) Perovskite Nanocrystals for Photodetector Application. *ACS Appl. Nano Mater.* **2020**, *3*, 11107−11117.
(41) Valakh, M. Y.; Lisitsa, M. P.; Trilis, A. V.; Yaremko, A. M.; Peresh, E. Y. Raman Scattering in A3B2C9 Ferroelectric Crystals. *Phys. Solid State* **1997**, *39*, 1289−1291.
(42) Akriti; Zhang, S.; Lin, Z. Y.; Shi, E.; Finkenauer, B. P.; Gao, Y.; Pistone, A. J.; Ma, K.; Savoie, B. M.; Dou, L. Quantifying Anionic Diffusion in 2D Halide Perovskite Lateral Heterostructures. *Adv. Mater.* **2021**, *33*, 1−11.
(43) Dai, S.; Fei, Z.; Ma, Q.; Rodin, A. S.; Wagner, M.; McLeod, A. S.; Liu, M. K.; Gannett, W.; Regan, W.; Watanabe, K.; Taniguchi, T.; Thiemens, M.; Dominguez, G.; Castro Neto, A. H.; Zettl, A.; Keilmann, F.; Jarillo-Herrero, P.; Fogler, M. M.; Basov, D. N. Tunable Phonon Polaritons in Atomically Thin van Der Waals Crystals of Boron Nitride. *Science (80-.).* **2014**, *343*, 1125−1129.
(44) Li, Z.; Sun, F.; Zheng, Z.; Chen, J.; Davydov, A.; Deng, S.; Zhang, H.; Chen, H.; Liu, F. High-Quality All-Inorganic Perovskite CsPbBr3Microsheet Crystals as Low-Loss Subwavelength Exciton−polariton Waveguides. *Nano Lett.* **2021**, *21*, 1822−1830.
(45) Li, J.; Yang, R.; Rho, Y.; Ci, P.; Eliceiri, M.; Park, H. K.; Wu, J.; Grigoropoulos, C. P. Ultrafast Optical Nanoscopy of Carrier Dynamics in Silicon Nanowires. *Nano Lett.* **2023**, *23*, 1445−1450.
(46) Hu, F.; Luan, Y.; Scott, M. E.; Yan, J.; Mandrus, D. G.; Xu, X.; Fei, Z. Imaging Exciton-Polariton Transport in MoSe 2 Waveguides. *Nat. Photonics* **2017**, *11*, 356−360.
(47) Fei, Z.; Scott, M. E.; Gosztola, D. J.; Foley, J. J.; Yan, J.; Mandrus, D. G.; Wen, H.; Zhou, P.; Zhang, D. W.; Sun, Y.; Guest, J. R.; Gray, S. K.; Bao, W.; Wiederrecht, G. P.; Xu, X. Nano-Optical Imaging of WS E2 Waveguide Modes Revealing Light-Exciton Interactions. *Phys. Rev. B* **2016**, *94*, 1−6.
(48) Hu, D.; Yang, X.; Li, C.; Liu, R.; Yao, Z.; Hu, H.; Corder, S. N. G.; Chen, J.; Sun, Z.; Liu, M.; Dai, Q. Probing Optical Anisotropy of Nanometer-Thin van Der Waals Microcrystals by near-Field Imaging. *Nat. Commun.* **2017**, *8*, 1471.

https://doi.org/10.1021/acs.nanolett.4c00327
Nano Lett. 2024, 24, 5182−5188